



Investigation of Cascadia segmentation with ambient noise tomography

Robert W. Porritt ^{a,*}, Richard M. Allen ^a, Devin C. Boyarko ^b, Michael R. Brudzinski ^b

^a Dept. of Earth and Planetary Science, UC Berkeley, USA

^b Dept. of Geology, Miami University, USA

ARTICLE INFO

Article history:

Received 26 March 2011

Received in revised form 23 June 2011

Accepted 24 June 2011

Available online 16 July 2011

Editor: P. Shearer

Keywords:

Cascadia
tomography
segmentation
episodic tremor and slip
arc volcanism
subduction zone structure

ABSTRACT

Along strike variation in the characteristics of subduction zone processes has been observed throughout the Cascadia Subduction Zone through magmas analysis of arc magmas and the distribution of seismicity. We investigate links between these observations and subduction zone structure by imaging three-dimensional lithospheric scale shear velocity with ambient noise tomography (ANT). The crustal portion of the model is well resolved through typical ANT processing techniques. We expand the methodology to use longer period phase velocities in order to recover structure to ~120 km depth. The resulting model, PNW10-S, represents structural information in terms of relative shear velocity in the crust and uppermost mantle. Crustal structure mirrors surface geology to ~10 km depth and then transitions to a structure that is dominated by the subducting slab. The subducting slab and overriding crust appear segmented into three parts with boundaries near 43°N and 46°N. This three-way structural segmentation is aligned with the variation in recurrence of episodic tremor and slip along the subduction zone. Upper to middle crustal boundaries between the Klamath Mountains and Siletzia Terrane (43°N) and between the Crescent Formation and Olympic Peninsula (47°N) are also coincident with locations of increased occurrence of tremors raising the question of whether there is a link between the intensity of tremor activity and shallow (<10 km) crustal structure. The slab–segment boundary at 43°N is a stronger feature than the northern segment boundary at 46°N and appears to be the continuation of the Blanco Fracture Zone separating the Gorda segment of the plate from the rest of the Juan de Fuca plate. The southern half of the arc system, south of 45°N, shows lower velocities from the surface to ~80 km depth relative to the northern portion of the arc. We propose that this is due to clockwise plate rotation, which causes extension in the south, and results in increased melting. Along the arc, four broad low-velocity features are imaged just below the Moho and centered at 42°N, 44°N, 47°N, and 49°N. We interpret these as ponding of melt just below the crust where differentiation can occur before further ascent through the crust.

Published by Elsevier B.V.

1. Introduction

The Cascadia Subduction Zone is where the last remnants of the Farallon Plate continue to subduct below continental North America (Van der Lee and Nolet, 1997). The southern terminus of the trench is the Mendocino Triple Junction, offshore northern California, and the northern terminus is the Queen Charlotte Triple Junction to the northwest of Vancouver Island (Fig. 1). The Juan de Fuca plate is small in a global context, but the length of the subduction zone is sufficient to generate magnitude 9 earthquakes (Goldfinger et al., 2011). The subduction zone is atypical for a variety of reasons. It has a distinct paucity of seismicity, with no earthquakes greater than ~75 km depth, and almost no sub-crustal earthquakes beneath Oregon. The trench is undergoing rollback and clockwise rotation as the Basin and Range

expands to the southeast (Humphreys and Coblenz, 2007). Finally, the subduction zone exhibits anisotropic fast directions normal to the trench as observed from shear wave splitting (Currie et al., 2004; Eakin et al., 2010), whereas the vast majority of subduction zones have trench-parallel fast directions (Long and Silver, 2008).

In this paper we employ ambient noise tomography to image the lithospheric structure of the Cascadia Subduction Zone from southern Vancouver Island to California. Ambient seismic noise tomography has been used to study several regions including the western United States (Moschetti et al., 2007), the eastern United States (Liang and Langston, 2008), Taiwan (Huang et al., 2010; You et al., 2010), Costa Rica (Harmon et al., 2008), Norway (Köhler et al., 2011), Australia (Saygin and Kennett, 2010), and Europe (Yang et al., 2007). Ambient noise is particularly useful in seismically quiescent areas because recovery is primarily influenced by receiver array geometry and not the distribution of earthquakes. We make use of seismic stations from the Earthscope Transportable Array, regional seismic networks, and two Earthscope Flexible Array deployments resulting in an array covering most the United States with greatly increased density in

* Corresponding author at: Dept Earth and Planetary Sciences, UC Berkeley, 307 McCone Hall, Berkeley, CA 94720, USA. Tel.: +1 906 281 3675; fax: +1 510 643 5811.
E-mail address: rwp@berkeley.edu (R.W. Porritt).

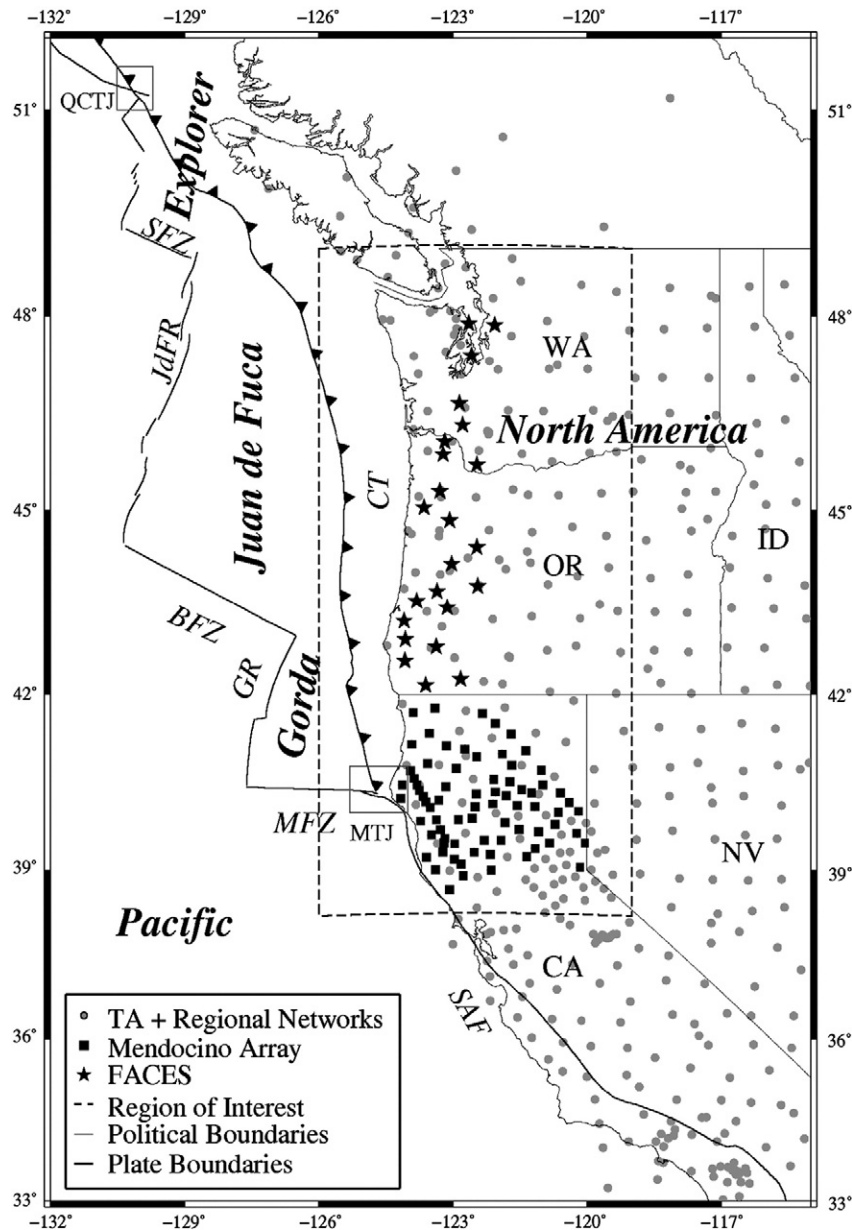


Fig. 1. Tectonic and station location map. The full station coverage extends to the eastern US coast and northwest to Alaska and includes the Earthscope Transportable Array, Regional Networks, and the Canadian National Network (gray circles). The densest coverage is in the Pacific Northwest due to the addition of the deployment of two temporary arrays, FACES and Mendocino (stars and squares respectively). Our region of focus (dashed box) covers the US portion of the Cascadia Subduction Zone and extends south of the Mendocino Triple Junction (MTJ) where the subduction zone terminates. Major plate boundaries labeled as follows: SAF – San Andreas Fault, MFZ – Mendocino Fracture Zone, GR – Gorda Ridge, BFZ – Blanco Fracture Zone, CT – Cascadia Trench, JdFR – Juan de Fuca Ridge, SFZ – Sovanko Fracture Zone, QCTJ – Queen Charlotte Triple Junction.

Cascadia (Fig. 1). The measurements typically derived from ambient noise are fundamental mode Rayleigh wave phase velocities between 7 and 40 s. These measurements have peak sensitivity between the surface and roughly 50 km depth and thus this method provides excellent sampling of the crust. In order to investigate the structure throughout and immediately below the lithosphere, we use measurements from noise cross-correlations to periods of 90 s. This requires manual data selection to ensure high signal-to-noise ratios. The benefit of this labor-intensive process is that the resulting model is able to resolve structure from the surface to ~120 km depth. It therefore provides the missing link between previous crustal studies (ambient noise, controlled source (Trehu et al., 1994), and seismicity studies) and the larger scale models using teleseismic surface- and body-waves, which have only longer wavelength or deeper sensitivity.

2. Cascadia segmentation

Several lines of evidence suggest that simple subduction with one downgoing and one overriding plate is an insufficient model of the Cascadia Subduction Zone. Instead, the subduction zone and arc are segmented, exhibiting variations in multiple characteristics along strike. A first order observation of this is the Sovanko and Blanco Fracture zones separating the Explorer and Gorda micro-plates from the main Juan de Fuca plate (Fig. 1). A similar scale feature is the distinct change in strike of the trench from nearly north–south in California and Oregon to northwest–southeast through northern Washington and Vancouver Island (Audet et al., 2010; McCrory et al., 2004). On a shallower scale, modeling of the GPS velocity field by McCaffrey et al., 2007 shows that the data is best fit by a series of crustal block motions rather than by pure plate motion based models.

The topography of the forearc provides further evidence of segmentation. The southern and northern ends of the subduction zone are mountainous, but the central region is relatively flat and low lying. The Klamath Mountains at the southern end of the subduction zone are composed of metamorphic oceanic rocks (Harden, 1998). The Olympic Peninsula at the northern end of the study region is also composed of metamorphic and sedimentary oceanic rocks (Brandon et al., 1998). However, the central lowland region is a mixture of sediment deposited from erosion of the Cascades Range and uplift of the Siletzia Terrane (McNeill et al., 2000). The mid-crustal portion of the Siletzia Terrane is considered to be a captured oceanic arc (Duncan, 1982) and is often mapped by its enriched chemistry (Schmidt et al., 2008) and high seismic velocities (Trehu et al., 1994).

Variations in seismicity suggest another form of segmentation. The subduction zone is atypical everywhere in that there are no seismic events below ~75 km depth anywhere along its length and thus the Wadati–Benioff zone is sparsely defined and shallow. There are a few subduction interface events deeper than the continental crust at the northern and southern ends of the subduction zone in Washington and California, but only to 75 km depth. However, there are almost no sub-crustal (>30 km depth) earthquakes beneath Oregon. In contrast, Episodic Tremor and Slip (ETS) events have been mapped throughout the subduction zone (Brudzinski and Allen, 2007). The recurrence rate of ETS, consisting of many non-volcanic (or tectonic) tremors at the same time as geodetically measured backslip (Rogers and Dragert, 2003), varies along strike (Brudzinski and Allen, 2007) with similar segment boundaries as observed by the variation in seismicity and topography.

Other evidence for segmentation along the arc comes from the composition of arc volcanism. Detailed analysis of primitive basalt families in the main volcanic arc reveals variable mantle domains and melting regimes attributed to the effects of the slab window to the south, impingement of the Basin and Range terrain, and interaction with the Siletzia Terrane (Schmidt et al., 2008). In addition, measurements of total heat production from volcanic fumaroles, thermal springs, and slightly thermal springs (Ingebritsen and Mariner, 2010) show significantly higher total heat production in the southern part of the arc where Basin and Range extension is thought to create permeable zones in the crust (Ingebritsen and Mariner, 2010).

3. Data and methodology

Our dataset focuses on two Flexible Array experiments, FlexArray along Cascadia Experiment for Segmentation (FACES) and the Flexible Array Mendocino Experiment (Mendocino), while also including data from the Berkeley BDSN, Canadian Seismic Network, USArray Transportable Array, and the Advanced National Seismic System (ANSS) backbone seismic network. We also include broadband stations from a total of 42 networks listed by network code in the acknowledgments resulting in a total of 1554 broadband stations. The dataset extends temporally from July 2007 through September 2010. While we focus on the Pacific Northwest, the dataset extends spatially throughout the entire United States with some coverage in Canada. The focus region and a broader subset of our station coverage are shown in Fig. 1.

We follow the method of Bensen et al. (2007) to compute empirical Green's functions (EGFs) from ambient noise cross correlations. For each broadband station, single day vertical component waveforms are time aligned, whitened to broaden the noise band, and filtered to isolate the fundamental mode Rayleigh wave between 5 and 150 s. The cross-correlation is then computed for each station pair and stacked for the time period when both stations are available. We then implement a frequency–time analysis (Dziewonski et al., 1969) with phase-matched filters (Levshin et al., 1989) to measure Rayleigh wave group and phase velocities from the EGFs.

The dominant source for the Rayleigh wave signal is the microseismic background noise (Bromirski et al., 2005; Landès et al., 2010). Microseismic noise is strongest near the primary and secondary microseisms at 16 and 8 s respectively (Cessaro, 1994), but broadly extends to 40 s (Peterson, 1993). We therefore treat the short period band (7–40 s) separately from the longer period (41–90 s) measurements. The short period phase velocities from 39 months of data (800,000 paths) are compared with a distribution of expected phase velocities (Fig. S1) computed from global and regional models including PREM (Dziewonski and Anderson, 1981), IASPI91 (Kennett and Engdahl, 1991), WUS (Pollitz, 2008), and GIL7 (Dreger and Romanowicz, 1994). The measurements are then required to exceed a variable threshold for signal-to-noise ratio (SNR) and wavelength dependent inter-station spacing. Those data that are within 1 SD of the expected value are given a relatively low threshold in both SNR and distance in order to be included in the later inversion, while those which fit within only 3 SD must satisfy a higher threshold to pass. Those that are outside 3 SD are rejected outright (see Table 1 for values).

The longer period measurements (45, 50, 55, 60, 65, 70, 80, and 90 s) are extracted from an 11-month, 200,000 path dataset. The 200,000 paths were manually graded based on the strength of signal in raw correlation and how well the dispersion curves fit to a reasonable distribution of phase velocities. This was facilitated through a Matlab gui which displays information about each station pair individually. This information included the inter-station distance and azimuth, the number of days stacked in the correlation, the names of the two stations, the symmetric cross correlation, the measured group and phase velocities, and the measured spectral SNR. The user could then input an acceptable bandpass and grade them as excellent, good, average, poor, or rejected. To achieve good or excellent grades, the correlation needed to show a clear dispersive waveform around 3 km/s and a relatively smooth and continuous dispersion curve. The paths were then further selected via similar threshold SNR and distance criteria (see Table 1) as the automatically selected short period measurements, but with the manual grade in place of the standard deviation. This manually intensive approach has little effect in the short period band, but drastically improves the recovery at periods greater than 40 s. Other studies (Calkins et al., in press; Yang et al., 2008) have incorporated measurements of phase velocity from earthquake-based methods. Both approaches are designed to stabilize the inversion at greater depths than are typically considered with ambient noise. In general, using earthquake derived long period phase velocities is preferable where available due to the time involved with the manual selection process.

The path integrated phase velocities are inverted for phase velocity maps using the method of Barmin et al. (2001). Smoothing and damping weights are constant for each period. The smoothing uses a

Table 1

(top) Parameters used in automatic selection of phase velocities for periods of 7–40 s. A measurement which fits within the number of standard deviations from the reference model (S1) in the first column must pass the minimum SNR and minimum number of wavelengths in columns 2 and 3 corresponding to that row, i.e. a measurement within 1 SD needs a minimum SNR of 5 and at least 2 wavelengths inter-station distance. (bottom) Parameters used for the hand-graded measurements.

	Min SNR	Min #wavelengths
<i>Standard deviations</i>		
1	5	2
2	20	3
3	30	4
4	30,000	40,000
<i>Manual grade</i>		
Excellent	2	1
Good	15	2
Average	20	3
Poor	30	4

correlation radius of one wavelength to reduce short-wavelength anomalies. Fig. S2a–e, f–j shows the phase velocity maps for both the hand-picked and auto-picked data at a range of periods, and a comparison with the phase velocity maps of Pollitz and Snoko (2010) (Fig. 2a–e, Fig. S2k–o) from earthquake-based measurements. The earthquake-based approach is well established for periods greater than ~ 18 s because those modes are strongly excited by teleseismic earthquakes. Ambient seismic noise is well established between 7 and 40 s as a source for seismic tomography (Bensen et al., 2007). The two methods agree well in their overlapping pass-band (18–40 s). But, as can be seen in Fig. S2, the hand-picked ANT dataset shows much greater similarity to the Pollitz and Snoko (2010) phase velocity maps than the auto-picked ANT data does at periods greater than 40 s. The auto-picked long period maps are therefore rejected because they are dominated by short wavelength features not present in earthquake-based measurements. In the final inversion we therefore use the auto-picked ANT phase-velocities at 7–40 s and the manually selected ANT phase velocities at 45–90 s (shown in Fig. 2f–j).

In the final step we invert the phase velocities at each location for isotropic shear velocity. The phase velocities are first corrected for variable crustal thickness using the method of Pollitz and Snoko (2010). A crustal thickness model (shown in Fig. 3) is interpolated from Audet et al. (2010) and Levander et al. (2007) with a minimum thickness of 10 km imposed. This model uses the detailed depth to mantle constraints of Audet et al. (2010) where the subducting plate is shallower than the continental Moho, and the Levander et al. (2007) constraints elsewhere. We then invert phase velocity perturbations using damped least squares and Frechet kernels computed for the reference 35 km crust (crustal thickness variability has already been accounted for in the corrections to the phase velocity measurements). The inversion is damped towards a global mean of zero. For presentation we remove a depth dependent mean value and apply a final smoothing function with 25 km radius.

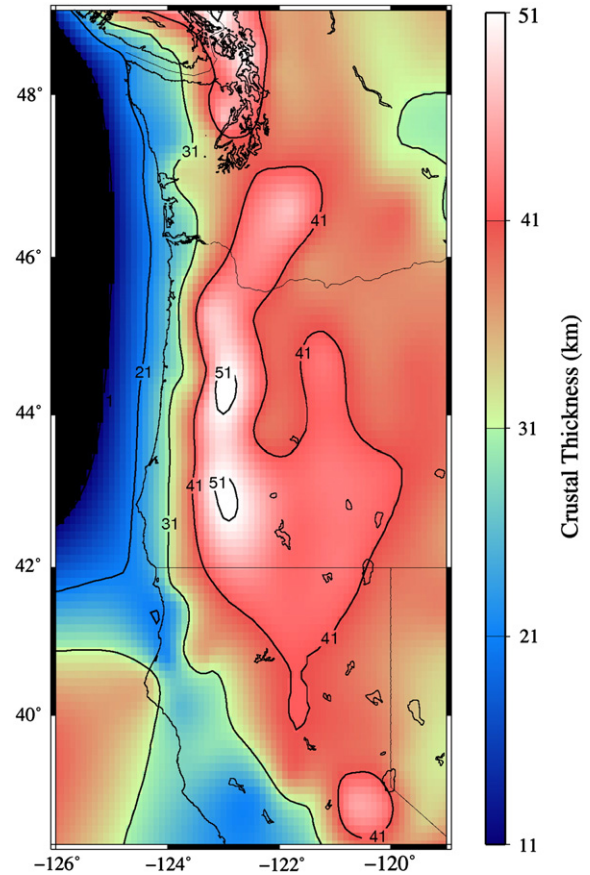


Fig. 3. Map of crustal thickness used in our starting model. This was generated using Audet et al. (2010) for the Moho of the subducting oceanic plate and Levander et al. (2007) for the continental Moho and imposing a 10 km minimum thickness.

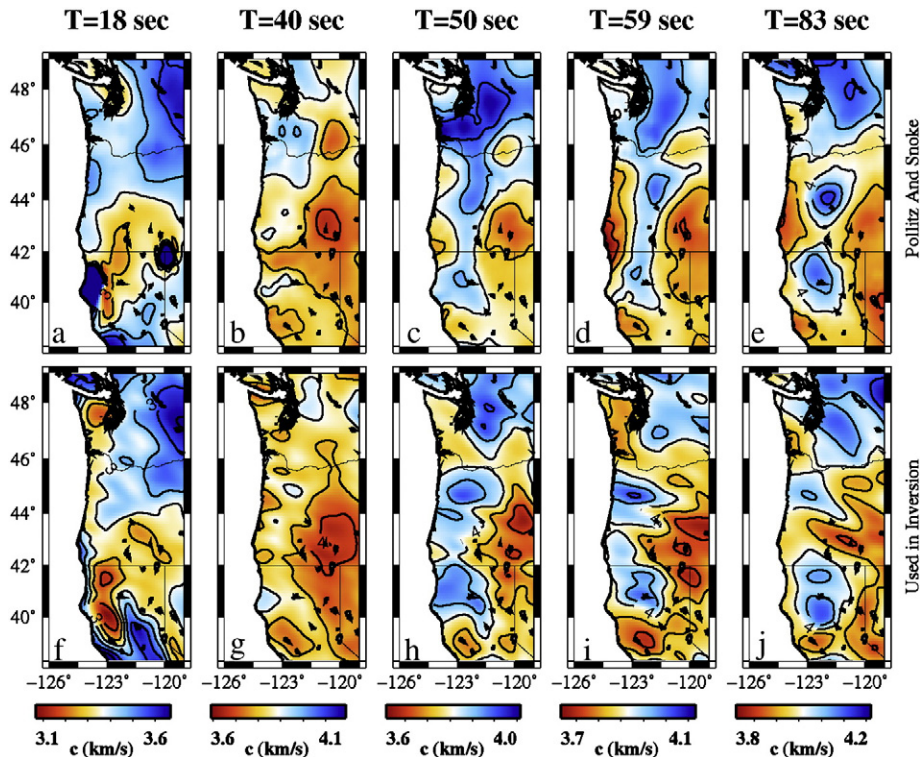


Fig. 2. Phase velocity maps at 18, 40, 50, 59, and 83 s. Each column is the same period with the same color scale. The top row (a–e) shows the phase velocity maps from Pollitz and Snoko (2010). The lower row (f–j) shows the chosen phase velocity maps used in our shear velocity inversion and are a combination of maps generated from automatically selected data at short periods (7–40 s), and manually selected data for longer periods (45–90 s).

4. Noise source distribution

The theoretical basis for noise correlations returning an accurate and stable estimate of the Green's function between two stations relies on the assumption of homogeneously distributed noise sources. Using a large number of inter-station paths, long time periods, and symmetric sided correlations helps satisfy this approximation, but there is still debate about the source distribution of microseismic noise and therefore its suitability as a source for tomography. The long period earth hum located by [Rhie and Romanowicz \(2004\)](#) shows the strongest energy is generated in the northern Pacific Ocean basin during the Northern Hemisphere winter and in the southern Pacific during the Southern Hemisphere winter. Other authors have located shorter period microseisms as a combination of deep-ocean and near shore sources ([Bromirski et al., 2005](#)). Recent observations by [Landès et al. \(2010\)](#) have identified compressional waves in the secondary microseismic band within noise correlations, which back-project to similar winter sources as the hum.

We follow the beam forming method of [Landès et al. \(2010\)](#) to locate the source of energy in the cross correlations between station pairs within the Mendocino experiment ([Fig. 1](#)). [Fig. 4](#) shows the azimuth of the peak energy from the center of the array in northern California for each month during the Mendocino Experiment. This shows the energy propagating to the northeast during the summer months and to the southeast in the winter months. Because the array is near a north–south trending coastline, a near coastal source should appear as nearly pure eastward propagating energy. Therefore it is more likely the energy is coming primarily from deep ocean activity during the winter months of the northern and southern hemisphere ocean basins. This implies that to maximize the distribution of noise sources in a measurement, the cross-correlation function should be computed over a period of ~1 or more years. Optionally, sampling evenly between a few winter and a few summer months may also achieve a reasonable distribution of noise sources.

5. Resolution

We address the resolution of the model in three ways. The first two concern the inversion from path-averaged phase velocity to phase velocity maps, while the third assesses the full methodology. In the

first approach we perform checkerboard resolution tests ([Fig. S3a–e](#)) at various periods to determine the ability of the data and inversion to resolve alternating high and low phase velocities. The recovery of these tests is dependent on both our ray-path coverage and chosen inversion parameters. To isolate the effect of the inversion parameters, we present an “Ideal Recovery” map ([Fig. S3a](#)) created by tracing 500,000 infinite frequency (thin) rays randomly generated in the model space through the input checkerboard with sides of $1.5 \times 1.5^\circ$ and inverting with our inversion parameters. In a perfect inversion, the sides of alternating anomalies would be straight lines. The recovered checkerboard maps for a set of periods (8, 20, 40, and 70 s) are shown in [Fig. S3b–e](#) to illustrate the effects of both the ray coverage and the inversion parameters for the given period. Largely the recovery is good, but the 70-second period map's amplitude recovery is reduced compared to the shorter periods. Further, note that the checkers nearest the coast are smeared west relative to the ideal recovery map, which indicates reduced path coverage along the coast.

The second approach we use is the method of [Barmin et al. \(2001\)](#), which defines resolution as the minimum distance (km) at which two delta functions can be uniquely identified. The approach results in a spatial function describing areas of better or poorer coverage with lower values indicative of better resolution. These maps are shown in [Fig. S4](#) for the same set of periods as the checkerboard test. These quantitative resolution maps show a decrease in resolution near the coasts and an overall reduction in the resolvable length-scale in the long period map which is reasonable for longer periods. Therefore deeper features near the coastlines cannot be considered fully resolved.

Finally we test the resolution of the full two-stage inversion approach by inverting our three-dimensional reference model. To create the reference model, we adjust the WUS model of [Pollitz \(2008\)](#), which has a 35 km Moho, to the Moho defined by our crustal thickness model at each spatial point. The three-dimensional shear velocity model is then converted to phase velocity for each period at each location by a propagator matrix method ([Shapiro and Ritzwoller, 2002](#)). The rays used in our inversion are then traced through the synthetic phase velocity model to generate “raw” synthetic phase velocity observations. These data are then inverted as with the real data; first to determine phase velocity maps, and then the phase

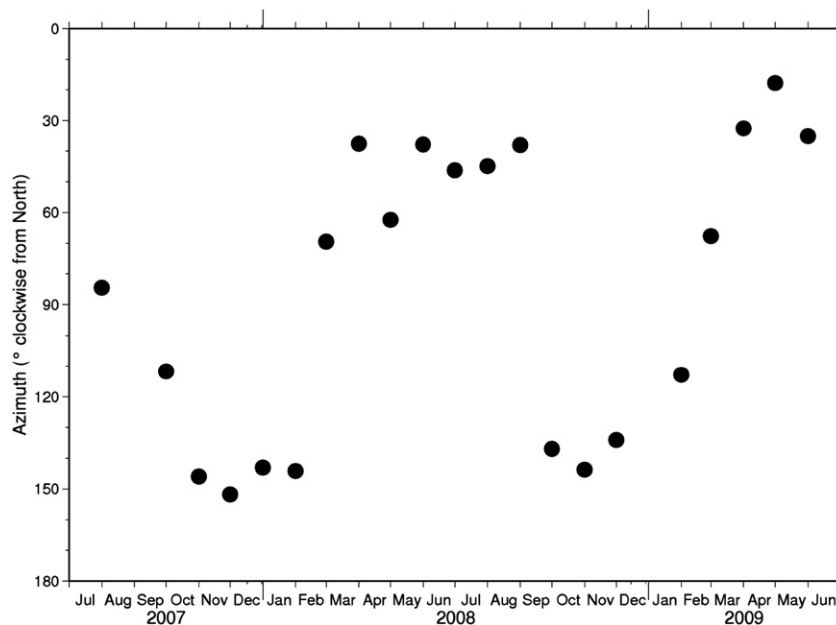


Fig. 4. Azimuth of the maximum energy propagation direction with velocity between 2 and 5 km/s as a function of time. This is derived from the Mendocino array over the duration of the experiment and shows that the energy comes from the southwest in the summer and the northwest in the winter.

velocity maps are inverted using the same damped least squares method to obtain relative shear velocity. A perfect inversion should yield zero anomalies everywhere, indicating we recover the reference model. Deviations from zero are therefore indicative of artifacts. As seen in Fig. S5, the magnitude of the anomalies resulting from this test is very small and significantly lower than those in the final model. The distribution of these features is also randomly distributed without structure correlated to structure in our model. This suggests that our model does not contain significant structural artifacts resulting from the processing. However, because low amplitude structure in our model may be false, we focus on only the high-amplitude anomalies in our following interpretation.

6. Results

Map sections of the resulting model, PNW10-S, are shown in Fig. 5 with surface features and tectonic observations illustrated to the left (Fig. 5a and e). Crustal structure is seen in Fig. 5b–d and mantle structure is shown in Fig. 5f–h. The shallowest image at 5 km depth shows structure similar to mapped geology with sedimentary areas imaged as low velocity regions and mountainous regions as high velocity regions. In the mid crust, at 10 km and 15 km depths, the structure shows only limited correlation with surface features.

The Columbia Basin appears as a strong low velocity in the 5 km and 10 km images. The Sierra Nevada and Central Valley are distinct high- and low-velocity anomalies, respectively, at 5 km depth. The southern Cascade Range appears slow in the crust, while the northern Cascade

Range is largely high velocity. The high velocity northern Cascade Range merges with the high velocity region in the mid crust below the Oregon Coast Range and the Willamette Valley to the west and the eastern section containing the Columbia River Basalt. The Olympic Peninsula appears as a low velocity package dipping to the west.

An approximately linear north–south striking feature dominates the deeper images beginning near the coast at 35 km depth and progresses eastward with depth. This is the subducting Juan de Fuca slab. At 35 km depth a predominantly slow anomaly is observed beneath the onshore region with the edge of a high velocity feature just visible along the coastline. At greater depth, a broader high velocity feature is observed with low-velocities to the east at each depth. The high-velocity slab is segmented into two or three zones. The southern segment boundary is visible in slices from 35 to 100 km depth and is near the California–Oregon border (42°N). A northern segment boundary is also observed in the 100 km image near the Oregon–Washington border (46°N). However, this boundary is less consistent at different depths. In the 100 km map, the high velocity anomaly is broadest which is probably due to the drop in resolution near the coast, particularly at longer wavelengths.

Fig. 6 shows a cross section through the southern portion of the subduction zone. Fig. 6a shows color scales of absolute velocity in the crust and relative velocity in the mantle. For comparison, Fig. 6b has the entire section in relative velocity. While both images display essentially the same structure, major features are more prominent in Fig. 6b and thus we use a relative velocity scale for the fence diagrams in Figs. 7 and 8 discussed below in Sections 7.1 and 7.2.

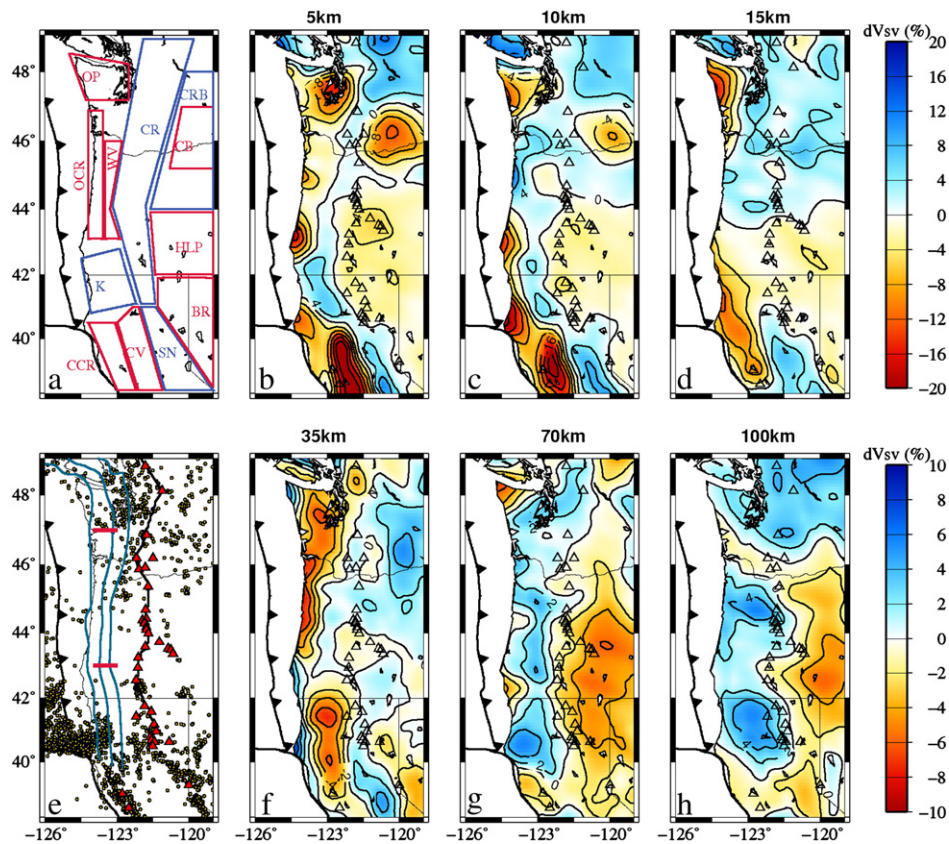


Fig. 5. (a and e) Tectonic maps of the study region. (a) Highlights crustal structure showing sedimentary regions in red and igneous/metamorphic regions in blue. OP – Olympic Peninsula, CR – Cascades Range, CRB – Columbia River Basalts, OCR – Oregon Coast Range, WV – Willamette Valley, CB – Columbia Basin, K – Klamath Mountains, HLP – High Lava Plains, BR – Basin and Range, CCR – California Coast Range, CV – Central Valley, SN – Sierra Nevada. (e) shows earthquakes since 1990 (gold dots), tremor segmentation bounds (red lines), volcanoes (red triangles), depth to slab contours at 20, 30, and 40 km from Audet et al. (2010) (blue lines), and the locations of profiles in Figs. 7 and 8. (b–d, f–i) Depth slices of PNW10-S at 5, 10, 15, 35, 70, and 100 km. Overlain on the depth slices are the quaternary volcanic centers as unfilled triangles.

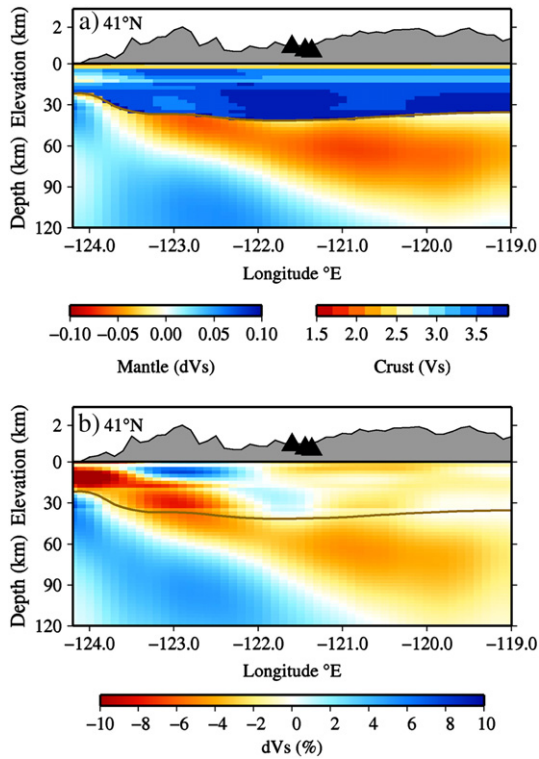


Fig. 6. Vertical east–west cross-sections of PNW10-S at 41°N through the Klamath Range. Panel 6a gives the best fit shear velocity in the crust and perturbation in the mantle. Panel 6b shows only relative velocity perturbations. In both cases the topography is shown in gray over the structure. Active Quaternary volcanoes within 30 km are overlain on topography and the Moho is overlain on the shear velocity structure. All depths and elevations are in km. Velocity scales are shown at the bottom of the figure.

7. Discussion

The continental crust is an amalgamation of multiple blocks that have been accreted to the continent. The Klamath Mountains are a crystalline block of oceanic material (Harden, 1998), which is relatively fast in the upper crust, but relatively slow in the deep crust. The high velocity mid-crust under central Oregon is the Siletzia Terrane (Snively et al., 1980). Above the Siletzia, the Oregon Coast Range and Willamette Valley are low velocity features. McNeill et al. (2000) reconstruct this as uplift of the Siletzia with older sedimentary cover and backfill of the basin with younger sediments. The Olympic Peninsula is a largely slow anomaly owing to a sedimentary and metamorphic core formed through a continuous mass recycling process in the accretionary wedge (Brandon et al., 1998). Furthermore, the Crescent formation basalts form a high velocity half ring on the eastern side of the sedimentary core, which is expected for the large basaltic feature (Babcock et al., 1992).

The crust of the Cascades Range shows a strong north–south dichotomy in terms of velocity structure with higher velocities in the north and lower velocities to the south. Ingebritsen and Mariner (2010) show a similar separation near 45.25°N based on the total heat production measured in hydraulic systems near volcanic centers. They interpret this as impingement of Basin and Range extension in the crust of the southern arc leading to more permeable pathways for fluid circulation. This coincides well with the low velocities imaged in the upper crust of the southern region. However, the imaged low velocities in the southern region extend to far greater depths than heated fluids could circulate (Saar and Manga, 2004). Thus we consider the large scale low velocity anomalies as regions of magmatic plumbing systems, but we are unable to uniquely constrain the dimensions of individual magma chambers due to the scale of our model and smoothing inherent in tomographic inversions.

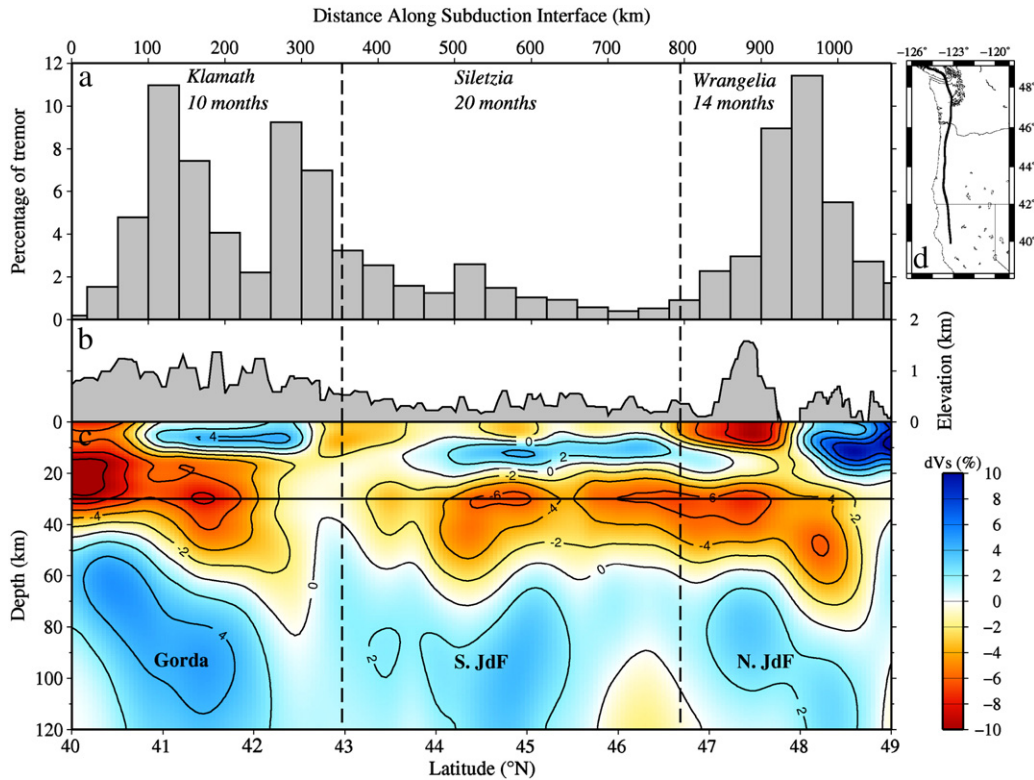


Fig. 7. Comparison of PNW10-S with characteristics of ETS. (a) Histogram showing variability in tremor occurrence along strike (Boyarko and Brudzinski, 2010). (b) Topography along profile. (c) Relative shear velocity structure along a profile where the slab is at 30 km depth (profile location shown in d). Vertical lines on profile at 43°N and 46.7°N indicate the tremor segmentation bounds of Brudzinski and Allen (2007) with the names and recurrence interval given. The horizontal line is the top of the ocean crust from Audet et al. (2010). Also labeled are the slab sections corresponding to the Gorda, Southern Juan de Fuca (S. JdF) and Northern Juan de Fuca (N. JdF).

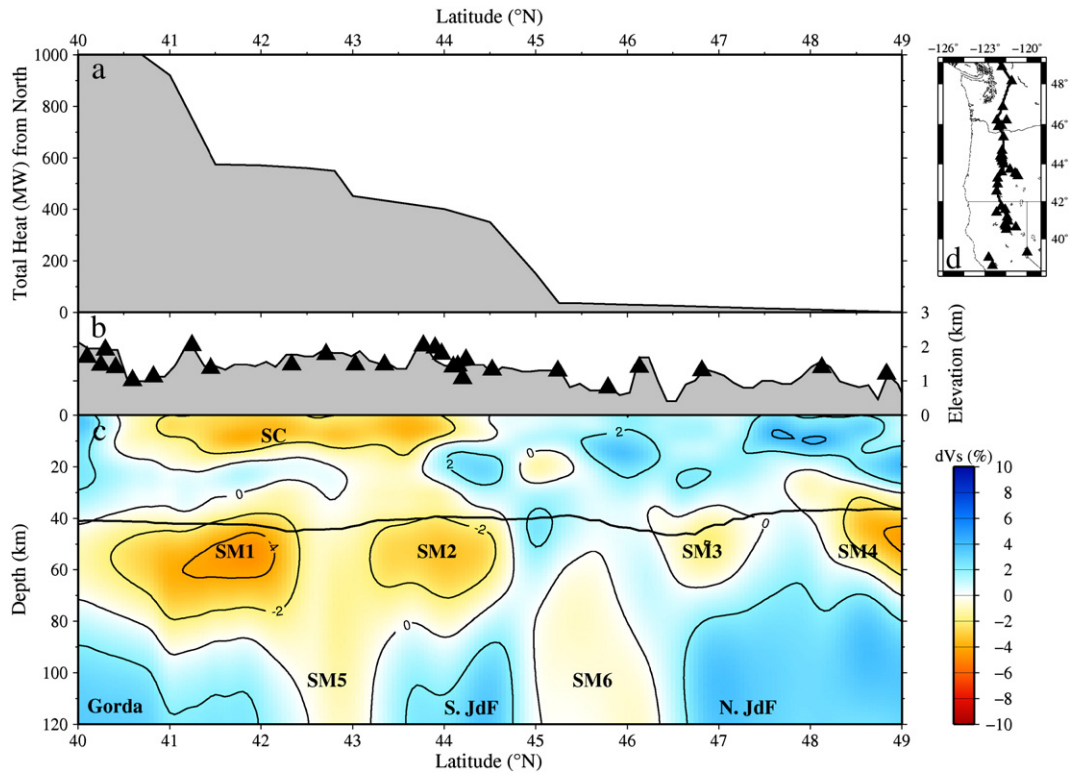


Fig. 8. Comparison of PNW10-S with heat production observations. (a) Cumulative heat production from the north to south along the arc (modified from Ingebritsen and Mariner, 2010). (b) Topography along profile with nearby volcanoes plotted as triangles. (c) Shear velocity structure along the profile that runs along the arc. Profile shown in the upper right (d). The black line around 40 km depth is the Moho. Major anomalies are labeled. Slow crust (SC) is the area of Basin and Range impingement. Slow mantles (SM1–4) are the interpreted ponded areas of melt. SM5 and SM6 are the plate segmentation boundaries separating the Gorda, Southern Juan de Fuca (S. JdF), and Northern Juan de Fuca (N. JdF).

The deeper structures (>30 km) can be readily interpreted in terms of subduction zone features. In the 35 km map, the Juan de Fuca plate appears as a relatively slow anomaly beneath onshore regions as we are imaging the subducting oceanic crust including sediments and possible fluids while the other material at that depth is either mantle peridotite or deep crustal granitoid with little water content. Low velocities above the plate interface may reflect fluid rich oceanic sediments being underplated to the continent as described in Calkins et al., in press. In the deeper images, the fast velocity is the subducting oceanic lithosphere, which is colder than the background mantle due to exposure near the surface. In the mantle, the slab appears segmented into at least two, and possibly three, sections with high velocity cores at 41°N, 45°N, and 47.5°N and reduced high velocities at the boundaries at 42°N and 46°N. The northern edge of the southernmost segment coincides with the landward continuation of the Blanco Fracture Zone near the California–Oregon boarder (42°N), and which separates the Gorda and Juan de Fuca sections of the subducting plate. Thus we interpret the southern slab segment as the Gorda micro-plate. The second segmentation boundary is near the Oregon–Washington border (46°N) where a low velocity corridor separates the central and northern segments. This northern segmentation boundary is less clear in our model, but similar to an area of reduced high velocity imaged in teleseismic body wave studies (Obrebski et al., 2010).

7.1. Implications for tremor

Brudzinski and Allen (2007) identify a variation in the recurrence interval of ETS along the arc with a recurrence interval of 14 months in the north, 20 months in the center, and 11 months in the south. We seek to expand on that observation by investigation of three-dimensional structure. ETS events are typically thought to occur on the plate interface (Brown et al., 2009; Ghosh et al., 2009; Shelly et al.,

2007) between 30 km and 45 km depth (Audet et al., 2010). The cross section in Fig. 7c is constructed by extracting the velocity values along a profile aligned to the 30 km slab contour from Audet et al. (2010), which is thought to represent the up-dip limit of ETS. Superimposed on this image are the long-term ETS segmentation boundaries at 43°N and 46.7°N (Brudzinski and Allen, 2007). These boundaries, based on the recurrence interval for ETS events, are aligned with both the location of the high velocity Siletzia Terrane in the mid-crust (~15 km depth) and also the deeper three-way segmentation in the subducting oceanic lithosphere between the Gorda, Southern Juan de Fuca, and Northern Juan de Fuca at 60–120 km depth as described above. Thus the segmentation of ETS is aligned with structural boundaries in both the continental crust and the subducting oceanic lithosphere.

The frequency of tremors along the strike of the subduction zone is shown in Fig. 7a (Boyarko and Brudzinski, 2010). The three peaks in the proportion of events around 41°N, 42.5°N, and 48°N do not correspond to peaks or troughs in topography or to significant structural anomaly centers of crustal or lithospheric blocks as imaged tomographically. However, they do correspond to regions with strong lateral gradients in the upper crust (0–15 km depth). This correlation between tremor frequency and near surface structure is surprising because tremor is believed to be occurring at greater depths. This may imply that the conditions for tremor generation are dependent on upper crustal structure whether they occur on the plate interface or throughout the continental crust (Kao et al., 2005).

7.2. Implications for volcanic activity

Fig. 8 shows a set of observations along the axis of the Cascades volcanic range. Fig. 8a is modified from Ingebritsen and Mariner (2010) showing cumulative heat production from the north to the south as measured from volcanic fumaroles, thermal springs, and slightly thermal springs. Comparing this to PNW10-S (Fig. 8c) shows a

strong correlation between the high heat production south of 45°N and a large zone of low velocities between 40.5°N and 45°N. The water-based measurements for the total heat production sample fluids circulating between 0 and 15 km depth (Saar and Manga, 2004) and thus Ingebritsen and Mariner (2010) interpret this high heat production zone as due to the influence of extension from the Basin and Range province creating permeable pathways for fluid flow in the upper crust. This helps explain the low velocity zone in the upper crust (Fig. 8c; anomaly SC), however the low velocity zone extends to ~80 km depth.

The extension of the Basin and Range, and the associated clockwise rotation of the Cascadia margin (Bates et al., 1981; McCaffrey et al., 2000), could explain the lower velocities in the southern half of the subduction zone at all depths (Fig. 8c; anomalies SM1, SM2, and SM5). The rotation leads to extension at the southern end, which promotes melting and results in the larger low velocity zone. The center of this low velocity zone is also located at the slab segmentation boundary (at 43°N, Fig. 8c, anomaly SM5) described earlier and associated with the continuation of the Blanco Fracture Zone separating the Gorda and Juan de Fuca portions of the plate. The Gorda portion of the plate is actively deforming to a much greater extent than the Juan de Fuca section to the north. This is evidenced by en echelon strike-slip seismicity throughout the plate, and the clockwise rotation of magnetic anomalies relative to the Gorda Mid-Ocean Ridge and also relative to the magnetic anomalies north of the Blanco Fracture Zone as seen in the North American Magnetic Anomaly Database (NAMAD, 2011). This may also imply increased rotation of the Gorda segment relative to the Juan de Fuca portion. This could promote separation of the Gorda and Juan de Fuca plates below the trench exposing more of the slab to hot mantle resulting in increased melting and further increased plate separation. The low velocity feature below 90 km which separates the slab segments at 43°N (anomaly SM5) may therefore be a channel feeding melt to the southern section of the arc. The other slab segmentation boundary discussed above is defined by the deep low-velocity anomaly between 45°N and 46°N (anomaly SM6). This feature is not coupled to broad low velocities beneath the arc. As described above, this segment boundary is less clearly defined in the tomography, and there is no association with differential deformation processes as in the case of the Gorda–Juan de Fuca. In the northern portion of the arc there is also reduced extension, which would not promote melting as it does to the south.

In addition to the large-scale north–south variability in the velocity structure beneath the arc, we observe four smaller-scale pockets of low velocity just below the Moho near 42°N, 44°N, 47°N, and 49°N (anomalies SM1, SM2, SM3, and SM4 respectively). These may be regions where melt is ponding and differentiation is occurring before the melt continues its path up through the crust. Evidence from Schmidt et al. (2008) suggests there are four distinct source regions for the arc melts along Cascadia and the boundaries that they identify correlate approximately with the locations of the four low-velocities at the base of the Moho. Recent numerical modeling by Karlstrom et al. (2009) describes how crustal magma chambers between the surface and 30 km depth grow by capturing feeder dikes from below the magma chamber. The individual crustal magma chambers are likely too small to be resolved by our tomography, but these broader low-velocity pockets below the Moho are likely the sources of the feeder dikes, which become captured in relatively discrete mid-crustal magma chambers before being erupted at the surface with the observed evidence of variable source characteristics.

8. Summary

By utilizing ambient noise tomography at longer periods than is typical (to 90 s), a single method based velocity model of the entire lithosphere is resolved allowing us to address questions relating to processes within the continental crust, and the relationship of these

processes to lithospheric-mantle structure and the underlying subducting oceanic crust and mantle in the Cascadia Subduction Zone. At shallow depths (5 km) the velocity structure correlates well with surface geologic observations as basins are imaged as low velocity features and mountain ranges show high velocities. Below ~10 km depth, structure transitions from a reflection of crustal blocks to structure dominated by the subducting slab at 70 km depth. The slab is imaged as a broad high velocity feature with a thin low velocity layer on top believed to be the subducting oceanic crust.

Episodic tremor and slip is observed along the length of Cascadia, but the characteristics vary along strike. The recurrence interval of ETS defines three zones along the arc with a recurrence interval of 14 months in the north, 20 months in the center, and 11 months in the south (Brudzinski and Allen, 2007). These three segments correlate well with several structures within PNW10-S. The three segments of the subducting plate align with the ETS segmentation, and the mid-crustal location of the Siletzia Terrane aligns with the region of 20-month recurrence. We also note that the three peaks in tremor activity are collocated with upper crustal lateral velocity gradients.

While the slab is imaged all along the Cascadia margin, it shows strong variability in structure. Three segments are apparent at 100 km depth, which is consistent with deeper structure (Obrebski et al., 2010). The southern segment appears to be an extension of the Gorda section of the plate implying that the continuation of the Blanco Fracture Zone below the trench is a weak zone allowing increased clockwise rotation of the Gorda slab and/or increased melting along its locus. The entire southern half of the arc (south of 45°N) is lower velocity than the northern half. Total heat production measurements (Ingebritsen and Mariner, 2010) show the same north–south divide and we observe lower velocities in the shallow crust (0–15 km depth), which correlates well with the higher heat production. While the lower crust shows no strong velocity anomalies, lower velocities are again seen below the Moho to a depth of ~80 km. We propose that increased melting along the extension of the Blanco Fracture Zone, promoted by the clockwise rotation of the arc and the associated extension in the south, is responsible for the lower velocities and increased heat production in the southern portion of the arc. We further note the location of four distinct pockets of low velocity just below the Moho. These are likely regions where melt is ponding and differentiating before the lighter components rise through the crust. These are likely the source of the feeder dikes drawn on by crustal magma chambers (Karlstrom et al., 2009).

Supplementary materials related to this article can be found online at doi: [10.1016/j.epsl.2011.06.026](https://doi.org/10.1016/j.epsl.2011.06.026).

Acknowledgements

Awards EAR-0643392, EAR-0745934, and EAR-0643077 from the National Science Foundation's Earthscope program funded this work. We would like to thank a multitude of fieldwork helpers involved with the FACES and Mendocino experiments including Hector Hinojosa, Eugene Humphreys, Alan Levander, Leland O'Driscoll, Pat Ryan, Stefany Sit, Andrew Tran, and Yongbo Zhai. All figures were made with GMT (Wessel and Smith, 1998). We thank Morgan Moschetti, Michael Ritzwoller, Anatoli Levshin, and Mikhail Barmin for providing FTAN and path tomography codes. We thank Mathieu Landes and Nikolai Shapiro for codes to calculate forward dispersion models and to locate energy in cross-correlations. We thank Oliver Kreylos and Louise Kellog for providing 3D Visualizer software used in our interpretation. Thanks to the PASSCAL Instrument Center for help installing and maintaining the stations as well as for helping process the data for archival at the IRIS DMC. Data was obtained from the IRIS DMC, the NCEDC NETDC for BDSN data, and the Canadian Seismic Network's AutoDRM from the Geological Survey of Canada for Canadian data. The networks providing data are: AZ, BK, CC, CI, CN,

CO, EP, ET, HW, II, IM, IU, IW, LB, LD, LI, NE, NM, NN, NR, PB, PE, PN, SC, TA, UO, US, UU, UW, WY, XC, XE, XQ, XR, XT, XU, XV, Y8, YU, YW, Z2, and ZG. Finally we thank Mathias Obrebski, Pascal Audet, Leif Karlstrom, and two anonymous reviewers for insightful comments.

References

- Audet, P., Bostock, M.G., Boyarko, D.C., Brudzinski, M.R., Allen, R.M., 2010. Slab morphology in the Cascadia fore arc and its relation to episodic tremor and slip. *J. Geophys. Res.* 115, B00A16. doi:10.1029/2008JB006053.
- Babcock, R.S., Burmester, R.F., Engebretson, D.C., Warnock, A., Clark, K.P., 1992. A rifted margin origin for the crescent basalts and related rocks in the northern coast range volcanic province, Washington and British Columbia. *J. Geophys. Res.* 97 (B5), 6799–6821. doi:10.1029/91JB02926.
- Barmin, M.P., Ritzwoller, M.H., Levshin, A.L., 2001. A fast and reliable method for surface wave tomography. *Pure Appl. Geophys.* 158 (8), 1351–1375.
- Bates, R.G., Beck Jr., M.E., Burmester, R.F., 1981. Tectonic rotations in the Cascade Range of southern Washington. *Geology* 9, 184–189.
- Bensen, G.D., Ritzwoller, M.H., Barmin, M.P., Levshin, A.L., Lin, F., Moschetti, M.P., Shapiro, N.M., Yang, Y., 2007. Processing seismic ambient noise data to obtain reliable broad-band surface wave dispersion measurements. *Geophys. J. Int.* 169, 1239–1260. doi:10.1111/j.1365-246X.2007.03374.x.
- Boyarko, D.C., Brudzinski, M.R., 2010. Spatial and temporal patterns of nonvolcanic tremor along the southern Cascadia subduction zone. *J. Geophys. Res.* 115, B00A22. doi:10.1029/2008JB006064.
- Brandon, M.T., Roden-Tice, M.K., Garver, J.I., 1998. Late Cenozoic exhumation of the Cascadia accretionary wedge in the Olympic Mountains, northwest Washington State. *Geol. Soc. Am. Bull.* v. 110 (n. 8), 985–1009. doi:10.1130/0016-7606.
- Bromirski, P.D., Duennebieber, F.K., Stephen, R.A., 2005. Mid-ocean microseisms. *Geochem. Geophys. Geosyst.* 6, Q04009. doi:10.1029/2004GC000768.
- Brown, J.R., Beroza, G.C., Ide, S., Ohta, K., Shelly, D.R., Schwartz, S.Y., Rabbel, W., Thorwart, M., Kao, H., 2009. Deep low-frequency earthquakes in tremor localize to the plate interface in multiple subduction zones. *Geophys. Res. Lett.* 36, L19306. doi:10.1029/2009GL040027.
- Brudzinski, M., Allen, R.M., 2007. Segmentation in episodic tremor and slip along Cascadia. *Geology* 35 (10), 907–910. doi:10.1130/G23740A.1.
- Calkins, J. A., Abers, G. A., Ekström, G., Creager, K. C., and Rondenay, S., in press. Shallow structure of the Cascadia subduction zone beneath western Washington from spectral ambient noise correlation. *Journal of Geophysical Research*. doi:10.1029/2010JB007657.
- Cessaro, R.K., 1994. Sources of primary and secondary micro-seisms. *Bull. Seismol. Soc. Am.* 84, 142–156.
- Currie, C.A., Cassidy, J.F., Hyndman, R.D., Bostock, M.G., 2004. Shear wave anisotropy beneath the Cascadia subduction zone and western North American craton. *Geophys. J. Int.* 157, 341–353. doi:10.1111/j.1365-246X.2004.02175.x.
- Dreger, D.S., Romanowicz, B., 1994. Source characteristics of events in the San Francisco Bay region. *U. S. Geol. Surv. Open-File Rept.* 94–176, 301–309.
- Duncan, R.A., 1982. A captured island chain in the coast range of Oregon and Washington. *J. Geophys. Res.* 87 (B13), 10,826–10,837. doi:10.1029/JB087iB13p10827.
- Dziewonski, A.M., Anderson, D.L., 1981. Preliminary reference Earth model. *Phys. Earth Planet. Inter.* 25 (4), 297–356.
- Dziewonski, A.M., Block, S., Landisman, M., 1969. A technique for analysis of transient seismic signals. *Bull. Seismol. Soc. Am.* 59, 427–444.
- Eakin, C.M., Obrebski, M., Allen, R.M., Boyarko, D.C., Brudzinski, M.R., Porritt, R., 2010. Seismic anisotropy beneath Cascadia and the Mendocino triple junction: interaction of the subducting slab with mantle flow. *Earth Planet Sci. Lett.* 297, 627–632.
- Ghosh, A., Vidale, J.E., Sweet, J.R., Creager, K.C., Wech, A.G., 2009. Tremor patches in Cascadia revealed by seismic array analysis. *Geophys. Res. Lett.* 36, L17316. doi:10.1029/2009GL039080.
- Goldfinger, C., Nelson, C.H., Morey, A., Johnson, J.E., Gutierrez-Pastor, J., Eriksson, A.T., Karabanov, E., Patton, J., Gracia, E., Enkin, R., Dallimore, A., Dunhill, G., Vallier, T., 2011. Turbidite event history: methods and implications for Holocene paleoseismicity of the Cascadia Subduction Zone USGS Professional Paper 1661-F, Reston, VA U.S. Geol. Surv. 178 pp., 64 Figures.
- Harden, D., 1998. *California Geology: Englewood Cliffs*. Prentice Hall, New Jersey. 479 pp.
- Harmon, N., Gerstoft, P., Rychert, C.A., Abers, G.A., Salas de la Cruz, M., Fischer, K.M., 2008. Phase velocities from seismic noise using beamforming and cross correlation in Costa Rica and Nicaragua. *Geophys. Res. Lett.* 35. doi:10.1029/2008GL03587.
- Huang, Y.-C., Yao, H., Huang, B.-S., van der Hilst, R.D., Wen, K.-L., Huang, W.-G., Chen, C.-H., 2010. Phase velocity variation at periods of 0.5–3.0 seconds in the Taipei basin of Taiwan from correlation of ambient seismic noise. *Bull. Seismol. Soc. Am.* 100 (no. 5A), 2250–2263. doi:10.1785/0120090319.
- Humphreys, E.D., Coblenz, D.D., 2007. North American dynamics and western U.S. tectonics. *Rev. Geophys.* 45, RG3001. doi:10.1029/2005RG000181.
- Ingebritsen, S.E., Mariner, R.H., 2010. Hydrothermal heat discharge in the Cascade Range, northwestern United States. *J. Volcanol. Geotherm. Res.* vol. 196 (Issues 3–4), 208–218. doi:10.1016/j.jvolgeores.2010.07.023 0377–0273.
- Kao, H., Shan, S.-J., Dragert, H., Rogers, G., Cassidy, J.F., Ramachandran, K., 2005. A wide depth distribution of seismic tremors along the northern Cascadia margin. *Nature* 436, 841–844. doi:10.1038/nature03903.
- Karlstrom, L., Dufek, J., Manga, M., 2009. Organization of volcanic plumbing through magmatic lensing by magma chambers and volcanic loads. *J. Geophys. Res.* 114, B10204.
- Kennett, B.L.N., Engdahl, E.R., 1991. Traveltimes for global earthquake location and phase identification. *Geophys. J. Int.* 122, 429–465.
- Köhler, A., Weidle, C., Maupin, V., 2011. Directionality analysis and Rayleigh wave tomography of ambient seismic noise in southern Norway. *Geophys. J. Int.* 184, 287–300. doi:10.1111/j.1365-246X.2010.04830.x.
- Landès, M., Hubans, F., Shapiro, N.M., Paul, A., Campillo, M., 2010. Origin of deep ocean microseisms by using teleseismic body waves. *J. Geophys. Res.* 115, B05302. doi:10.1029/2009JB006918.
- Levander, A., Niu, F., Miller, M.S., Zhai, Y., Liu, K., 2007. USArray receiver function images of the lithosphere in the western U.S. *EOS Trans* 88.
- Levshin, A.L., Yanovskaia, T.B., Lander, A.V., Bukchin, B.G., Barmin, M.P., Ramikova, L.I., 1989. In: Keilis-Borok, V.I. (Ed.), *Surface waves in vertically inhomogeneous media, in Surface Waves in a Laterally Inhomogeneous Earth*, pp. 131–182.
- Liang, C., Langston, C.A., 2008. Ambient Seismic Noise Tomography and Structure of Eastern North America. doi:10.1029/2007JB005350. vol. 113, B03309.
- Long, M.D., Silver, P.G., 2008. The subduction zone flow field from seismic anisotropy: a global view. *Science* 319, 315–318.
- McCaffrey, R., Long, M.D., Goldfinger, C., Zwick, P.C., Nabelek, J.L., Johnson, C.K., Smith, C., 2000. Rotation and plate locking at the Southern Cascadia Subduction Zone. *Geophys. Res. Lett.* 27 (19), 3117–3120.
- McCaffrey, R., Qamar, A.I., King, R.W., Wells, R., Khazaradze, G., Williams, C.A., Stevens, C.W., Vollick, J.J., Zwick, P.C., 2007. Fault locking, Block Rotation and Crustal Deformation in the Pacific Northwest. *Geophysical Journal International*. doi:10.1111/j.1365-246X.2007.03371.x.
- McCrory, P.A., Blair, J.L., Oppenheimer, D.H., Walter, S.R., 2004. Depth to the Juan de Fuca slab beneath the Cascadia subduction margin – a 3-D model for sorting earthquakes. *U.S. Geological Survey Data Series* v.91 version 1.2.
- McNeill, L.C., Goldfinger, C., Kulm, L.D., Yeats, R.S., 2000. Tectonics of the Neogene Cascadia forearc drainage; investigations of a deformed late Miocene unconformity. *Geol. Soc. Am. Bull.* 112, 1209–1224.
- Moschetti, M.P., Ritzwoller, M.H., Shapiro, N.M., 2007. Surface wave tomography of the western United States from ambient seismic noise: Rayleigh wave group velocity maps. *Geochem., Geophys., Geosys.* 8, Q08010. doi:10.1029/2007GC001655.
- NAMAD, North American Magnetic Anomaly Database, May 28th, 2011. http://crustal.usgs.gov/projects/namad/the_project.html May 28th, 2011 accessed.
- Obrebski, M., Allen, R.M., Xue, M., Hung, S.-H., 2010. Slab–plume interaction beneath the Pacific Northwest. *Geophys. Res. Lett.* vol. 37, 114305. doi:10.1029/2010GL043489 6 pp., 2010.
- Peterson, J., 1993. Observation and modeling of seismic background noise. *U.S. Geol. Surv. Tech. Rept.* 93–322 1–95.
- Pollitz, F., 2008. Observations and interpretation of fundamental-mode Rayleigh wavefields recorded by the Transportable Array (USArray). *J. Geophys. Res.* 113, B10311. doi:10.1029/2007JB005556.
- Pollitz, F.F., Snoke, J.A., 2010. Rayleigh-wave phase-velocity maps and three-dimensional shear velocity structure of the western US from local non-plane surface wave tomography. *Geophys. J. Int.* 180, 1153–1169. doi:10.1111/j.1365-246X.2009.04441.x.
- Rhie, J., Romanowicz, B., 2004. Excitation of Earth's continuous free oscillations by atmosphere–ocean–seafloor coupling. *Nature* 431, 552–556.
- Rogers, G., Dragert, H., 2003. Episodic tremor and slip on the Cascadia subduction zone. The chatter of silent slip: *Science* 300, 1942–1943. doi:10.1126/science.1084783.
- Saar, M.O., Manga, M., 2004. Depth dependence of permeability in the Oregon Cascades inferred from hydrogeologic, thermal, seismic, and magmatic modeling constraints. *J. Geophys. Res.* vol. 109 (no. B4), B04204. doi:10.1029/2003JB002855.
- Saygin, E., Kennett, B.L.N., 2010. Ambient seismic noise tomography of Australian continent. *Tectonophysics* 481, 116–125. doi:10.1016/j.tecto.2008.11.013.
- Schmidt, M.E., Grunder, A.L., Rowe, M.C., 2008. Segmentation of the Cascades Arc as indicated by Sr and Nd isotopic variation among diverse primitive basalts. *Earth Planet. Sci. Lett.* 266, 166–181. doi:10.1016/j.epsl.2007.11.013.
- Shapiro, N.M., Ritzwoller, M.H., 2002. Monte-Carlo inversion for a global shear velocity model of the crust and upper mantle. *Geophys. J. Int.* 151, 88–105.
- Shelly, D.R., Beroza, G.C., Ide, S., 2007. Non-volcanic tremor and low-frequency earthquake swarms. *Nature* 446 (7133), 305–307. doi:10.1038/nature05666.
- Snively Jr., P.D., Wagner, H.C., Lander, D.L., 1980. Interpretation of the Cenozoic geologic history, central Oregon continental margin. Cross-section summary: *Geol. Soc. Am. Bull.* 91, 143–146.
- Trehu, A.M., Asudeh, Brocher, T.M., Luetgert, J.H., Mooney, W.D., Nabelek, J.L., Nakamura, Y., 1994. Crustal architecture of the Cascadia forearc. *Science* 266, 237–243.
- Van der Lee, S., Nolet, G., 1997. Seismic image of the subducting trailing fragments of the Farallon plate. *Nature* 386, 266–269. doi:10.1038/386266a0.
- Wessel, P., Smith, W.H.F., 1998. New, improved version of the Generic Mapping Tools released, *EOS Trans.* AGU 79, 579.
- Yang, Y., Ritzwoller, M.H., Levshin, A.L., Shapiro, N.M., 2007. Ambient noise Rayleigh wave tomography across Europe. *Geophys. J. Int.* 168 (1), 259.
- Yang, Y., Ritzwoller, M.H., Lin, F.-C., Moschetti, M.P., Shapiro, N.M., 2008. The structure of the crust and uppermost mantle beneath the western US revealed by ambient noise and earthquake tomography. *J. Geophys. Res.* 113, B1231.
- You, S.-H., Gung, Y., Chiao, L.-Y., Chen, Y.-N., Lin, C.-H., Liang, W.-T., Chen, Y.-T., 2010. Multiscale ambient noise tomography of short-period Rayleigh waves across northern Taiwan. *Bull. Seismol. Soc. Am.* 100 (6), 3165–3173.